

A Fractal Analysis of the HI Emission from the Large Magellanic CloudBruce G. Elmegreen¹, Sungeun Kim^{2,3}, Lister Staveley-Smith⁴**ABSTRACT**

Fourier transform power spectra of the distribution of neutral hydrogen emission in the Large Magellanic Cloud is approximately a power law over ~ 2 decades in length. Power spectra in the azimuthal direction look about the same as the rectilinear spectra. No difference is seen between power spectra of single channel maps and power spectra of either the peak emission map or the integrated emission map at the same location. There is a slight steepening of the average 1D and 2D LMC power spectra at high spatial frequencies. Delta-variance methods also show the same power-law structure.

These results suggest that most of the interstellar medium in the LMC is fractal, presumably the result of pervasive turbulence, self-gravity, and self-similar stirring. The similarity between the channel and integrated maps suggests they cover about the same line-of-sight depth. The slight steepening of the power spectra at high spatial frequency, corresponding to wavelengths smaller than ~ 100 pc, could mark the transition from large-scale emission that is relatively shallow on the line of sight to small-scale emission that is relatively thick on the line of sight. Such a transition, if real, would provide a method to obtain the thickness of a face-on galactic gas layer.

To check this possibility, three dimensional fractal models are made from the inverse Fourier transform of noise with a power-law cutoff. The models are viewed in projection with a Gaussian density distribution on the line of sight to represent a face-on galaxy disk with finite disk thickness. The density structure from turbulence is simulated in the models by using a log-normal density distribution function with a scale factor dependent on the Mach number. Additional density structure from simulated HI phase transitions is included in some models. After tuning the Mach number, galaxy thickness, and mathematical form of the phase transition, the models can be made to reproduce the observed LMC power spectra, the amplitude of the HI brightness fluctuations, and the probability distribution function for brightness. In all cases, the HI structure arises from a relatively thin layer in the LMC; the thick part of the HI disk has little spatial structure. The large amplitude of the observed intensity variations cannot be achieved by turbulence alone; phase transitions are required.

The character of the fractal HI structure in the LMC is viewed in another way by comparing positive and negative images of the integrated emission. For the isotropic fractal models, these two images have the same general appearance, but for the LMC they differ markedly. The

¹IBM Research Division, T.J. Watson Research Center, P.O. Box 218, Yorktown Heights, NY 10598; e-mail: bge@watson.ibm.com

²Astronomy Department, University of Illinois at Urbana-Champaign, IL 61801

³Harvard Smithsonian Center for Astrophysics, 60 Garden Street, Cambridge, MA 02138; email:skim@cfa.harvard.edu

⁴Australia Telescope National Facility, CSIRO, PO Box 76, Epping, NSW 1710, Australia; email lstavele@atnf.csiro.au

HI is much more filamentary in the LMC than in an isotropic fractal, making the geometric structure of the high-emission regions qualitatively different than the geometric structure of the low-emission (intercloud) regions. The high-emission regions are also more sharply peaked than the low-emission regions, suggesting that compressive events formed the high-emission regions, and expansion events, whether from explosions or turbulence, formed the low-emission regions.

The character of the structure is also investigated as a function of scale using unsharp masks and enlargements with four different resolutions. The circular quality of the low emission regions and the filamentary quality of the high emission regions is preserved on scales ranging from several tens to several hundreds of parsecs.

The spatial scales for sources of turbulent energy input may be illustrated by rms variations in the power spectra with position in the galaxy. This rms decreases from ~ 0.6 at kpc scales to ~ 0.25 on ~ 20 pc scales. The large scale variations are probably from known supershells. The smaller scale variations could be the result of a combination of turbulent cascades from these large-scale energy inputs and additional energy sources with smaller sizes.

Subject Headings: turbulence – ISM: clouds – ISM: structure – galaxies: ISM – Magellanic Clouds

1. Introduction

Power spectra of HI in the Small Magellanic Cloud show a power law decrease with increasing wavenumber over 2.3 decades in length (Stanimirovic et al. 1999). Box-counting techniques and perimeter-area measures of the HI in M81 group galaxies indicate a scale-free behavior there too, over 1.7 decades (Westpfahl et al. 1999). These results for whole galaxies extend to much larger scales the fractal nature of interstellar gas that was previously found in Milky Way clouds using the same methods of power spectra (Crovisier & Dickey 1983; Green 1993; Lazarian & Pogosyan 2000; Stutzki et al. 1998) and perimeter-area correlations (Falgarone, Phillips, & Walker 1991). The similarity of these gas structures to the distribution of smoke particles and other passive tracers in incompressible laboratory turbulence (Sreenivasan 1991) and to the distribution of density in simulations of compressible turbulence (Elmegreen 1999; Rosolowsky et al. 1999; MacLow & Ossenkopf 2000; Pichardo et al. 2000) imply that turbulence is an important structuring agent for gas on a wide range of scales in a galaxy disk. Most of the galactic gas could be fractal as a result of this turbulence, producing both clouds with their power-law mass spectra (Elmegreen & Falgarone 1996; Stutzki et al. 1998) and the low density intercloud medium (Elmegreen 1997).

This paper applies a power spectrum analysis to HI emission from the Large Magellanic Cloud using the combined Australia Telescope Compact Array (ATCA) interferometric survey of HI by Kim et al. (1998a,b, 1999) and a single dish survey done with the Parkes Multibeam by Staveley-Smith et al. (in preparation). The combined data set is described by Kim et al. (2000). Because the HI is more structured in the LMC than the SMC as a result of supershells (Meaburn 1980, Kim et al. 1999) and other effects of star formation, we examine both local and global power spectra from one dimensional cuts in right ascension and declination, as well as power spectra in the azimuthal direction. We also determine the more conventional 2D power spectrum and Delta-variance for the whole LMC. The results are compared with power spectra in the same field from foreground Milky Way gas. A model fractal medium is used to comment on the implications of the observations.

One of the results of this work is that the structure of HI in the LMC is not a simple fractal like that obtained from fractal Brownian motion models (e.g., Stutzki et al. 1998). The geometry of the high

temperature emission is distinctly different from the geometry of the low temperature regions. Moreover, the extremes in HI brightness are too large to be reproduced by a realistic isothermal turbulence model. Rather, the ISM looks like a self-similar superposition of shells and filaments, separated by roundish holes. The contrast between the emission regions and the holes seems to require at least two phases of gas, such as the warm and cool phases of HI. In this respect, the LMC resembles computer simulations by Wada, Spaans, & Kim (2000). These simulations reproduce the large shells and the amorphous structures that are between the shells. Similar models and a more detailed study of the energy input from overlapping shells were made by Scalo & Chappell (1999a,b).

2. Data Source

The ATCA was used in the mosaic mode to survey a region $10^\circ \times 12^\circ$ covering the LMC, and at an angular resolution of $1'$, corresponding to a spatial resolution of 15 pc (for an assumed distance of 50 kpc). The detailed observations and data reduction are described in Kim et al. (1998a,b). The ATCA data for the LMC have been combined with Parkes single-dish data in order to add the low spatial frequencies missed by the interferometer (Kim, Staveley-Smith & Sault 2000). The Parkes observations were taken with the inner 7 beams of the Parkes Multibeam receiver (Staveley-Smith et al. 1996) in December 1998. The telescope has a half-power beamwidth of $14'.1$. A total bandwidth of 8 MHz was used with 2048 spectral channels in each of two orthogonal linear polarizations. The velocity spacing of the multibeam data is 0.82 km s^{-1} , but the final cube was Hanning-smoothed to a resolution of 1.6 km s^{-1} . The velocity range in the trimmed final cube is -66 to 430 km s^{-1} with respect to the barycentric reference frame. The pixel size in the final maps used here is $40''$, corresponding to $\sim 10 \text{ pc}$.

The shortest baseline (30 m) of the ATCA and the diameter (64 m) of the Parkes telescope provides an excellent overlap in the Fourier domain, allowing adequate cross-calibration of data from the two sources. The calibration agrees to within a few percent of the prediction (Kim et al. in preparation).

3. Analysis

The HI emission maps of the LMC show a complex structure composed of holes, filaments, and clumps, all with a wide range of scales. A previous analysis by Kim et al. (1999) of the holes and shells in the HI distribution found evidence for expansion around many of these sources, with a correlation between the expansion speed and the size of the shell that was consistent with energy input from visible massive stars. However, the majority of emission regions are not so clearly identified with energy sources. There is a lot of amorphous structure between the shells, some of which is filamentary, and much of this could be caused by random compressive events related to supersonic turbulence.

Turbulence produces a fractal-like pattern (Mandelbrot 1983) in which large regions are broken up into smaller regions, and these are broken further into even smaller regions, producing an overall hierarchy of structures. It is not possible to isolate individual “clouds” in such a structure without introducing some type of bias about what a cloud is and about how nested clouds should be counted. A better way to analyze this emission is with Fourier transform power spectra (PS), defined as the sum of the squares of the real and imaginary parts of the Fourier transform of the emission map, plotted versus the wavenumber, $k = 2\pi/\lambda$ for wavelength λ of certain features. Power spectra indicate the relative importance of features of various sizes. If a structure has no dominant scale, as would be the case for a perfect fractal, then the PS would

be a power law without kinks or features either. For an emission region of this type, the structure cannot be characterized as consisting of discrete and isolated clouds with certain sizes, but should be viewed as amorphous with a measurable parameter equal to the slope of the PS.

Fourier transform power spectra have been used to analyze HI structure in the local Galaxy by Crovisier & Dickey (1983) and Green (1993). They found power-law behavior indicative of a scale-free emission distribution. Analogous techniques have been applied to molecular data by Stutzki et al. (1998), who also got a scale free result. The first power spectrum study of a whole galaxy was by Stanimirovic et al. (1999) who used the ATCA + Parkes data of the Small Magellanic Cloud. Here we perform similar analyses of the LMC data from this same telescope combination.

In what follows, the power spectra for the LMC and foreground Galactic emission are presented in Section 3.1. The implications for the line-of-sight distribution and depth of the HI, and for the scale of turbulent energy sources, are discussed in Sections 3.2 - 3.4. Power spectra in the azimuthal direction are presented in Section 3.5, and two-dimensional power spectra, along with the two-dimensional Delta-variance, are in Section 3.6.

Power spectrum and Delta-variance analyses of spatially limited maps can introduce errors if there are sharp edges, but when the emission tapers off slowly toward the edges, as it does for whole galaxies like the LMC, then these problems are minimal. Power spectra of azimuthal profiles have no edge effects either. For this reason, our main results are not affected by map-edge effects. The only discussions where these effects might be important are those involving the 3×3 segments of the whole galaxy, which are used to determine rms variations with position, and those involving Milky Way emission on the line of sight to the LMC.

Fourier transform power spectra have other limitations too. Section 3.7 shows the LMC data in a different way to illustrate something that does not appear in the power spectra, namely the different topologies of the cloud and intercloud regions. The cloudy or high-brightness regions tend to be filamentary, while the intercloud or low-brightness regions tend to be round. Section 3.8 also shows another feature of the self-similar geometry using unsharp masks with four different scales of smoothing.

3.1. Power Spectra

Fourier transform power spectra (PS) were made of the channel maps, peak temperature map, and velocity-integrated map of HI emission from the Large Magellanic Cloud. Figure 1 shows the corresponding emission distributions. Each panel contains a field comprised of 600 pixels in the North-South direction by 630 pixels in the East-West direction, in addition to subfields measuring 200×210 pixels, indicated by white lines. The pixel size in the figures is $40''$; note that the beam size is $60''$ and the original sampling interval was $20''$. The map in the top left shows the peak temperature, the top right shows the velocity-integration, the lower left is the $v = 254 \pm 0.8 \text{ km s}^{-1}$ channel and the lower right is the $302 \pm 0.8 \text{ km s}^{-1}$ channel. Nine other channel maps were examined too, with 16 km s^{-1} spacing, and found to give similar results to the 254 and 302 km s^{-1} maps. The long stream of emission south of 30 Doradus is brighter on the integrated map than the peak temperature map because of its larger linewidth compared to the rest of the galaxy; it may contain a contribution from material that is not in the disk.

These images are optimized for the display of features and are not calibrated with a linear conversion between intensity and darkness. The conversion is close to linear, but the faint gray scales are highlighted a bit. For calibrated HI maps, see Kim et al. (2000).

Figures 2 and 3 show 1D power spectra for the LMC maps. Each PS is the average of many one-dimensional PS taken for the horizontal rows of pixels in the corresponding field. Solid lines are for the peak temperature data, dashed lines are for the integrated data, dot-dashed lines are for the 302 km s^{-1} channel and dotted lines are for the 254 km s^{-1} channel. For the 3×3 subfields of the galaxy shown in the corresponding 3×3 panels of Figure 2, the PS of each 210-pixel row was obtained from the FFT of the intensity using the IBM ESSL subroutine library, and then the PS from all 200 rows were averaged together to give the plotted result.

The same 210×200 field size was used for a sky region northeast of the galaxy. The sky region is shown on the integrated map in Figure 4, and the sky PS is shown in the left panel of Figure 3. This sky PS indicates the noise level for most of our study. At all but the highest frequencies, the noise contributes only a percent or less to the PS signal.

The middle panel in Figure 3 shows the average of the 1D power spectra for the whole galaxy field, made by averaging 600 power spectra from the 630-pixel-long FFTs of the horizontal rows. The right panel shows the average 1D power spectrum taken in a vertical direction, i.e., using 600 FFTs of 630-pixel long columns in the north-south direction (and using a different LMC boundary than what Fig. 1 shows, i.e., 600×630 pixels compared to 630×600 pixels).

The absolute brightnesses of the channel, peak temperature, and integrated maps are all different, so Figures 2 and 3 normalize the PS to lie at approximately the same height for easy comparison. The greater linewidth of the field south of 30 Dor gives it a larger ratio of integrated emission to peak temperature than the other fields, so the PS of the integrated emission south of 30 Dor shifts upward compared to the PS of the peak emission in this region.

The wavenumber ranges for all of the power spectra in figures 2 and 3 are also normalized so that image variations on a pixel scale are on the right-hand side of each abscissa at a normalized spatial frequency of 1, while variations on larger scales are on the left of each abscissa, at fractional normalized wavenumbers. The wavelength corresponding to a particular spatial frequency k equals $2/k$ pixels, which is about $20/k$ parsecs, as shown on the top axes. Thus each of the 3×3 panels in Figure 2 have PS that extend from a 20 pc scale on the right of the abscissa to a $105 \times 20 = 2100$ pc scale near the left of the abscissa. The middle and right panels of Figure 3 go to $3 \times$ larger spatial scales, so the PS extend further to the left in the plots.

Power spectra of foreground HI emission is shown in Figure 5. The three solid lines are the power spectra for HI emission in 200×220 pixel fields on the same line of sight as the LMC but at different velocities, covering foreground emission from the Milky Way. The dashed line is the PS from the peak temperature map of the LMC. The Milky Way emission has been divided by 40 to place the PS in about the same range as the peak temperature PS. The foreground emission has a PS that curls up at large spatial frequency, presumably from noise. The Milky Way emission has a generally steeper slope as well. Other correlation studies of high-latitude Galactic gas based on IRAS observations are in Abergel et al. (1996).

3.2. Channel Maps the same as Integrated Maps

Figures 2 and 3 contain several interesting results. First, the power spectra of the channel maps are essentially the same as the power spectra of the peak temperature and integrated maps in the directions where the channel emission originates. For example, most of the emission from the Northeast subfield is near 302 km s^{-1} , so the PS of the peak or integrated maps are about the same as the PS of the channel

map in the top left of the 3×3 panels. Similarly, most of the emission in the Southwest is near 254 km s^{-1} , so the PS of that channel is similar to the PS of the peak temperature or integrated maps in the lower right of the 3×3 panels.

This agreement between channel PS and peak-T or integrated PS occurs even though the channels are only a small part of the total emission. The implication of this result is that essentially all of the structure on a wide range of scales contributes equally to the channel maps at the velocity representative of the centroid speed of that region. The high velocity tail of the whole line spectrum does not, for example, contain only the small scale features. If it did, then the channel at the centroid would have relatively stronger large scale structure than the integrated map.

A related result is that the channel map cannot represent any thinner emission on the line of sight than the peak-T or integrated maps. Here, thinner is in the sense defined by Lazarian & Pogosyan (2000) as representing a spatial extent on the line of sight that is much smaller than the wavelength of the PS in the plane of the sky. If a channel map were thin in this sense, and the peak-T and integrated maps were not, then the PS of the channel map would be flatter than the PS of the peak-T or integrated maps (Lazarian & Pogosyan 2000). Since the PS are all about the same, the channel maps have emission from about the same line-of-sight depth as the integrated map.

The same is true for the peak-T and integrated maps: the similarity of their power spectra over all spatial frequencies means that they are either both shallow or both thick on the line of sight. For example, the peak temperature emission does not come from a thin midplane and the integrated emission from a thick disk.

3.3. Steepening at High Spatial Frequency as Evidence for Finite Disk Thickness

The power spectra of the LMC are approximately power laws in two separate segments, with a larger slope at larger spectral frequencies. This is not the case for the Milky Way power spectra, which have a constant slope (cf. Fig. 5). The curvature with increasing slope in the LMC PS is consistent with a prediction made by Lazarian & Pogosyan (2000) that the slope of a power spectrum should be steeper if the emission comes from a relatively thick line of sight, meaning one with a spatial thickness much larger than the transverse wavelength. Lazarian et al. predict a slope of $-11/3$ in thick regions and $-8/3$ in thin regions for *two* dimensional power spectra. These slopes increase by 1 to $-8/3$ and $-5/3$ for *one*-dimensional PS, which is appropriate for the present study. In fact, the slopes in Figures 2 and 3 equal these two values, with a steepening from $-5/3$ at low spatial frequency to $-8/3$ at high frequency. This implies that the shortest wavelengths studied here are significantly smaller than the line-of-sight thickness of the HI layer in the Large Magellanic Cloud. The larger wavelengths where the PS is shallow should be larger than the disk thickness. If this explanation for the PS steepening is correct, then we are measuring for the first time the line-of-sight depth of a gas layer in a galaxy.

The steepening transition for the power spectra of the LMC occurs at a wavelength of 80-100 pc. This is smaller than the expected thickness of a dwarf galaxy but perhaps not unreasonable for the LMC. Dwarf galaxy thickness are several hundred parsecs (Hodge & Hitchcock 1966; van den Bergh 1988; Staveley-Smith et al. 1992; Carignan & Purton 1998). For the LMC, Wang & Helfand (1991) estimate on the basis of a supershell model for LMC2 that the thicknesses of the cool HI cloud layer and the warm HI diffuse layer are 0.7 times the corresponding thicknesses in the Milky Way. This makes the cool cloud scale height 95 pc and the warm diffuse scale height 350 pc. The full disk thicknesses would be twice these values. Kim et

al. (1999) estimate an HI scale height of ~ 180 pc for the LMC using dynamical parameters that have been determined for the HI disk. This derived scale-height is consistent with an apparent distinction between giant shells and supergiant shells on a plot of velocity versus radius (Kim et al. 1999).

Our HI observations come from a mixture of cool and warm HI blended into a single spectral line, so a direct comparison with these thicknesses is not possible at this time. Model power spectra from layers with finite thicknesses are presented in Section 4. They suggest that most of the HI *structure* arises in a thin layer, presumably from the cool component of the HI, while the thicker, warmer component of the HI contributes little to these PS. This result is consistent with the observations of dwarf galaxies DDO 69 and Sag DIG by Young & Lo (1996, 1997), who found a low velocity dispersion (3.5 km s^{-1}) from presumably cool HI in the central or clumpy parts of the galaxies, and a high velocity dispersion (9 km s^{-1}) from presumably warm HI elsewhere. Most of the ISM structure is likely to be in the cool phase because this compresses most easily. If this cool phase has a low cloud-to-cloud velocity dispersion, then it should lie close to a galaxy’s midplane.

There are several other ways to check if PS steepening is sensitive to the disk thickness. First, the PS of whole-galaxy molecular maps should have a steepening transition at a higher spatial frequency than the PS for the HI because the molecular layer is probably thinner than the HI layer, as observed for the Milky Way. Second, the wavelength at the steepening transition should increase in the outer part of a face-on spiral galaxy where the outer HI layer flares. Similarly, the wavelength at PS steepening should decrease for inner galaxy disks if the scale height there is smaller as a result of the higher disk surface gravity. Higher resolution and lower noise observations of the LMC should help clarify this point as well, because they will extend the steep portion of the PS further to higher frequencies.

The relatively steep slope of the power spectrum for the Milky Way emission in Figure 5 implies that the emitting region is physically thick there too, compared to the transverse wavelength. For an average Milky Way distance of ~ 200 pc on the line of sight, the longest transverse wavelength is ~ 100 pixels, or ~ 7 pc. Thus the emission contributing to each channel has to have a depth on the line of sight that is larger than this.

A different explanation for the steepening of the LMC power spectrum at high spatial frequency is that the smallest clouds become optically thick and appear smooth. In this case, the power spectrum for the total column density could continue to decrease as a power law out to higher frequencies than measured here, but the substructure below ~ 100 pc may become washed out by the opacity effects, and cause the power spectrum to drop faster.

3.4. Spatial Variations in the Power Spectra as Evidence for Localized Energy Input

The variations of the PS from subfield to subfield are not noticeable in Figure 2 for scales less than ~ 200 pc. Larger scales have obvious variations. To study the variations better, Figure 6 plots the relative rms deviations between subfields of the peak temperature map, given as the rms between all of the nine power spectra, normalized to the average power spectrum. The relative rms variation decreases slightly with wavenumber, from ~ 0.4 to ~ 0.25 , suggesting that field-to-field variations are slightly larger for longer wavelengths. It is still relatively high at all wavelengths, though, as if no particular wavelength dominates the field variations.

We experimented with these rms variation by adding different amounts of noise to the HI peak

temperature map. Random noise added to each pixel caused the power spectrum to curl upward at high frequency, with a greater curl for higher-amplitude noise. This curl reflects the increasing power at high frequency that comes directly from the noise. However, the power spectrum for each of the 3x3 subfields curled up by about the same amount, and this caused the relative rms variation from subfield to subfield to decrease with increasing noise. We conclude from this experiment that noise in the data is not seriously affecting the rms variations of the power spectrum from subfield to subfield. In addition, the average noise level in the observations is typically less than 10% of the peak temperature for most regions. This is too small to account for the spatial variations in the power spectra. Thus, these variations are most likely the result of random positionings for real features in the maps.

The gradual decrease in subfield variations with wavenumber suggests that energy is put in at long wavelengths to varying degrees in different fields. This is consistent with the haphazard placement of giant shells throughout the LMC. The similarity of the PS for all of the fields at shorter wavelengths implies either that additional energy is put in uniformly over a wide range of scales, or that the large-scale energy cascades quickly and uniformly to smaller scales in each neighborhood.

3.5. Power Spectra in the Azimuthal Direction

Radial disk gradients and the disk edge in the LMC may affect the PS at large scales, so we removed any gradients by taking Fourier transforms of intensity scans in the deprojected azimuthal direction. Figure 7 shows the average PS of azimuthal scans from discrete radial intervals. Radius is measured on the major axis, and the deprojection assumes an inclination angle of 22° and a position angle of the line of nodes equal to 150° from vertical in the map. Each PS is the average of many PS, one for each pixel increment in radius within a range of radii centered on the value indicated for each line in the figure. The intensity at each azimuthal and radial position was determined by interpolation from the Cartesian grid of intensities in the original map. The left-hand panel in the figure is for the peak temperature map, and the right-hand panel is for the velocity-integrated map. The PS for an azimuthal scan at very large radius, 9.3 kpc, which is presumably in the sky region, is shown as a dotted line at the bottom of each panel. The abscissa is normalized as in Figures 2 and 3: single pixel fluctuations are plotted on the right edge, where the relative spatial frequency equals 1, and longer wavelengths relative to this are plotted toward the left. The longest wavelength increases with galactocentric distance as the physical length of the circumference increases. The radial intervals were chosen so that the number of points in the azimuthal scans were permissible ranges for FFT's in the IBM ESSL Fortran library.

The PS of the azimuthal scans in Figure 7 show the same steepening at large frequency as the PS of the horizontal or vertical scans in Figures 2 and 3. Each PS looks about the same, aside from seemingly random fluctuations at a level of about ± 0.4 dex at low wavenumbers, decreasing to ± 0.2 dex at large wavenumbers. This decrease is similar to that shown in Figure 6 and may result from enhanced energy input on large scales.

There is a slight change in the frequency of the break point as the radius of the azimuthal scan increases, from perhaps 80 pc wavelength at small radius to 150 pc wavelength at large radius. This increase could be the result of an increase in disk thickness with radius, as commonly observed in galaxies.

3.6. Two-Dimensional Power Spectrum and Delta Variance

Figure 8 shows the two-dimensional power spectrum of the central 630×630 pixel region ($\sim 6.3 \times 6.3$ kpc) of the integrated HI map of the LMC. The plotted quantity is the sum of the squares of the real and the imaginary parts of the 2D FFT made with the IBM ESSL subroutine package SRCFT2, averaged over each 2D wavenumber, $k = (k_x^2 + k_y^2)^{1/2}$. The result is a power law with a slightly steepening slope, as indicated by two lines. The overall power-law behavior is similar to that found by Stanimirovic et al. (1999) for the 2D power spectrum of the SMC, but the slight steepening here was not found there and is similar to that in the 1D power spectrum. The slope of the 2D power spectrum exceeds the average slope of the 1D power spectrum by about 1, as expected for the higher dimension.

The two-dimensional Delta variance discussed by Stützki et al. (1998) and Zielinsky & Stützki (1999) is shown in Figure 9. This quantity is given by

$$\sigma_{\Delta}^2(L) = \int_{3L/2}^{630-3L/2} dx_0 \int_{3L/2}^{630-3L/2} dy_0 \int_0^{3L/2} dr \left([I(x_1, y_1) - \langle I \rangle] \odot [|r\{x_0, y_0\} - r\{x_1, y_1\}|] \right)^2 \quad (1)$$

for function

$$\odot(r) = \pi (L/2)^{-2} \times \{1 \text{ for } r < L/2, \text{ and } -0.125 \text{ for } L/2 < r < 3L/2\}. \quad (2)$$

In this expression, the average intensity in the map is denoted by $\langle I \rangle$; $r(x_0, y_0)$ is the position of point (x_0, y_0) on the map, and $r(x_1, y_1)$ is the position of point (x_1, y_1) on a small region around (x_0, y_0) ; the distance between these two points is $|r\{x_0, y_0\} - r\{x_1, y_1\}|$.

For the Delta variance, the length L is measured in pixels in powers of 2, from 2 to 64 pixels. Thus the $L = 2$ case is like the integral over an unsharp mask made by taking the difference between an average over a circle 1 pixel in radius, and the average over the non-overlapping parts of a circle 3 pixels in radius; the $L = 64$ case is about as big as we can get, coming from the difference between a radius-32 circle and the non-overlapping radius-96 circle. The part of the whole map that is used for this integral, i.e., from $3L/2$ to $630 - 3L/2$ pixels, decreases with L in order to avoid spillover when the larger circle is subtracted.

The Delta variance is expected to be a power law if the power spectrum is a power law. The slope of the Delta variance on a log-log plot versus L should be smaller than that of the power law on a log-log plot versus $1/k$ by exactly 2. This is about right in the figures here. The slope of the power law on a log-log plot versus $1/k$ is 3.16, whereas the slope of the Delta variance on a log-log plot versus L is ~ 1 .

One advantage of the Delta variance over the power spectrum is that the delta variance can avoid the image edges, while the power spectrum assumes the image repeats itself infinitely in a periodic fashion. This difference can be important for an image with sharp edges, but for the case of a whole galaxy, where the edge tapers off gradually, the difference should not be physically significant. Our method to avoid the edges with the Delta variance contains an error of its own in that we consider different sub-parts of the whole galaxy for different scales L . Because the delta variance comes out to an approximate power law with the right slope compared to the power spectrum slope, the edge effects are not critical. The dotted line in figure 16 below demonstrates this point in a different way.

3.7. Filaments in the LMC

A qualitative aspect of the HI distribution in the LMC that cannot be obtained from power spectra is its filamentary nature. This is evident from the emission maps in Figure 1, and is a well-known property of

HI in the Milky Way (Kulkarni & Heiles 1987).

This filamentary structure becomes obvious if we compare positive and negative images of the HI emission in Figure 10. The lower panel shows the HI emission from a central region of the LMC as a bright white color on a blue background. The top part of the figure shows the HI emission as a blue color on a white background. The two parts of the figure look qualitatively different because the HI emission is filamentary and the regions between the HI emission, which are the intercloud medium, are more globular. That is, the white features in the bottom figure are filamentary, while the white features in the top figure are globular; this is true even though these are exactly the same figure with only the colors reversed. A similar plot (not shown) of a purely fractal cloud looks qualitatively the same in each color scheme.

The emission regions are also more sharply peaked than the valleys between them. Figure 11 shows a horizontal intensity trace 400 pixels long that comes from the middle of the lower figure in Figure 10. The trace is shown in both linear and logarithmic plots. The linear plot has sharp maxima and shallow minimum, whereas the logarithmic plot has more uniform sharpnesses for the maxima and minima.

The distribution function for the pixel-by-pixel values of intensity in a 400×400 pixel region centered on the LMC field shown in figure 10 is plotted on the left in Figure 12 using log-linear, linear-linear, and log-log coordinates. The bottom panel shows that the pixel values have an approximately Gaussian emission distribution. The curves on the right are from a model and will be discussed Sect. 4.

3.8. Unsharp Masks of the HI Emission

Another aspect of HI gas structure is the possibility that the morphology is different on different scales. The large scale seems to be dominated by a few giant shells, whereas the small scale seems filamentary in some images. We can check this impression by plotting unsharp masks of the data with different scales of smoothing, and then comparing these to enlarged versions of the highest resolution mask, enlarged to give the same number of pixels as the unsharp masks. If the enlarged version of a small region shows the same character of structure as an unsharp mask of a large region, blurred to the same number of pixels, then the structure is qualitatively self-similar on the two different scales.

Figure 13 shows unsharp masks of the whole LMC, using a 630×630 pixel field of view. The images were made as follows: first, each pixel of the integrated LMC map was replaced by the average of the surrounding $N_1 \times N_1$ pixels. This made a blurred map. Then another blurred map was made from averages over $N_2 \times N_2$ pixels. The final unsharp mask image is the difference between these two blurred maps.

In Figure 13, the panel in the top left was made from the difference between 3×3 and 11×11 maps; the top right is the difference between 11×11 and 41×41 maps, the bottom left is the difference between 21×21 and 81×81 maps, and the bottom right is the difference between 41×41 and 161×161 maps. Thus the images highlight structures on scales of 3, 11, 21, and 41 pixels. Recall that each pixel is about 10 pc for the LMC. There is no significant error from overflow outside the image in the figure because there is high-quality data from sky regions outside the galaxy for all of the pixels used in these unsharp masks (e.g., Fig. 4).

Figure 14 repeats the top left image from Figure 13 and also shows enlarged images of this map from the same position. The enlargements are by factors of $11/3$, $21/3$, and $41/3$, which means that the enlarged structures from the highest-resolution unsharp masked image have the same number of pixels as the smoothed structures in the three unsharp masked images. The enlarged images have the same character

of structure as the corresponding unsharp masked images, although not the same total range of intensities. The overall structure may be characterized as having holes with filamentary emission regions surrounding them. This implies that the geometry of the structure is qualitatively self-similar on the range of scales covered, which corresponds to 30 pc for the 3×3 pixel unsharp mask image to 410 pc for the 41×41 image. The self-similarity could persist up to even larger scales, but boundary effects make it hard to get a smoothed background on these larger scales for subtraction in the mask.

The range of intensities for the unsharp masked and enlarged images is different. There is no analogy to the extremely bright region south of 30 Dor in the enlarged region.

4. Fractal Emission Models

4.1. Model Setup

The wide range of scales that is observed for interstellar structures has led to a fractal model, starting with early observations of dust clouds (Beech 1987; Bazell & Désert 1988; Scalo 1990), molecular clouds (Dickman, Horvath, & Margulis 1990; Falgarone, Phillips, & Walker 1991), local atomic clouds (Vogelaar & Wakker 1994), and more recently, the ionized intercloud medium (Berkhuijsen 1999) and whole galaxies (Stanimirovic et al. 1999; Westpfahl et al. 1999). Computer simulations of supersonic turbulence also have a scale-free or fractal quality (Elmegreen 1999; Rosolowsky et al. 1999; MacLow & Ossenkopf 2000; Pichardo et al. 2000).

Because we observe a scale-free quality to the HI emission from the Large Magellanic Cloud, from both power spectra and unsharp masks, we would like to model the LMC with an idealistic fractal that is reasonably close to what might be expected from turbulence. By varying the line of sight depth and other properties of the model and fitting the resultant map to the LMC observations, we might be able to measure specific properties of the observed interstellar gas.

With this in mind, we made three-dimensional models of a fractal gas using a technique pioneered by Voss (1988). In this method, random complex-number noise in 3D wavenumber space is multiplied by a power law, and then the inverse Fourier transform is taken to give a fractal distribution in real 3D space. To reproduce something like the density structure that is expected from turbulence, we did two special things. First, the power law multiplier in wavenumber space was taken to be $k^{-5/3}$ for 3D wavenumber k . Second, after the 3D inverse Fourier transform was taken, the resulting pixel values, X , were exponentiated, making a 3D cube of values given by $\exp(\zeta X)$ instead of just X . This second step produces a 3D fractal with a near-power law power spectrum, and also with a probability distribution function of density (= final pixel values) that is log-normal. Such a log-normal pdf for density has been obtained from 3D numerical simulations of MHD turbulence (Vazquez-Semadeni 1994; Scalo et al. 1998; Nordlund & Padoan 1999).

We infer from the results in Nordlund & Padoan (1999) that the coefficient in the exponent, ζ , should be related to the Mach number, M , as:

$$\zeta = \frac{(\ln [1 + 0.5M^2])^{0.5}}{X_0}. \quad (3)$$

This relation arises as follows: the distribution function of pixel values that return from the inverse Fourier transform of the noise is found to be approximately a Gaussian, $\exp(-0.5 [X/X_0]^2)$, with a dispersion in the cases we ran equal to $X_0 = 1.27$. We use this fact to associate X with the log of the density, writing for

probability functions:

$$P_{\ln \rho}(\ln \rho) d\ln \rho = P_X(X) dX = e^{-0.5(X/X_0)^2} dX. \quad (4)$$

With $\zeta X = \ln \rho$, this becomes

$$P_{\ln \rho}(\ln \rho) = e^{-0.5(\ln \rho / [\zeta X_0])^2} \frac{dX}{d\ln \rho} = e^{-0.5(\ln \rho / \sigma)^2} \frac{1}{\zeta}, \quad (5)$$

where $\sigma = \zeta X_0$ is the dispersion of the pdf for density. This dispersion has been found by Nordlund & Padoan (1999) to be $\sigma = (\ln[1 + 0.5M^2])^{0.5}$, from which equation 3 follows.

Numerical simulations suggest that the density distribution function has a log-normal form only for isothermal turbulence, and that a power law function might be better for other cases (Scalo et al. 1998). One of the reasons for this is that a power law has much more structure at high densities than a log-normal, and this is the result of the presence of dense cool clouds in a non-isothermal model. With only one phase of matter in the isothermal case, the density cannot have such large variations at modest Mach numbers. The difference between these two cases has not been recognized yet from real power spectrum data, although we know that the ISM in the LMC does have two phases of HI from other studies (Marx-Zimmer et al. 2000). In what follows, we demonstrate that the structure of the ISM in the LMC requires more than isothermal turbulence. We do this by first obtaining an absurd result when the above model based on isothermal turbulent structure is assumed. We then modify the model to simulate two phases and obtain a nice fit to the observations.

Various values of the Mach-number parameter ζ were used in different models, along with various line-of-sight depths to an integral over the fractal density distribution, in an attempt to fit both the observed power spectrum of the LMC and the amplitude and character of the intensity trace shown in Figure 11. We used $\zeta = 1, 3, 5$, and 9 to simulate different Mach numbers and therefore different compressions from turbulence. For the model intensity, we "observed" the density distribution by integrating along one dimension of the model fractal, taken to represent distance on the line of sight. To simulate the thin disk of a galaxy, the 3D fractal was multiplied by a Gaussian centered on the middle pixel of the line of sight and having a scale height H . This represents a Gaussian ISM in a face-on galaxy, and the integral over this dimension represents the velocity-integrated spatial map. To compare with the observations of the LMC, we took 1D power spectra of the model map, averaged over all horizontal strips.

Several maps were made with various H . All had total transverse dimensions of 720×720 pixels, of which only the central 630×630 pixels were used for the power spectrum analysis, to avoid possible edge effects. This size is comparable to the total field size of the LMC map used for the power spectrum analysis in section 3.1 (the LMC field size was 630×600 , with the 630-pixel dimension in the direction of the one-dimensional power spectrum).

The depth of the 3D density distribution was always 60 pixels, which is the largest size that could fit in the memory of a single node of our computer, considering the other dimensions were 720×720 . In one case, only the central pixel was taken for the sky map, and in other cases, Gaussian multipliers for the fractal density distributions on the line of sight were used with Gaussian dispersions of $H = 0.125, 0.5, 2$, and 8 pixels.

A spatial map for the $\zeta = 5, H = 2$ case is shown on the top of figure 15. This case is chosen for display because it is a good fit to the power spectrum given in the next sub-section. Considering the pixel size in the LMC map, this $H = 2$ case corresponds to a scale height for the fractal structure of ~ 20 pc. On the bottom of figure 15 is the same map multiplied by an exponential with four scale lengths out to the edge.

This is meant to simulate the exponential disk in a real galaxy. The purpose of this exponential model is to demonstrate that edge effects in the sharp-edged fractal models do not cause the observed curvature and bends in the LMC power spectra (see next sub-section).

4.2. One dimensional Power Spectra and Intensity Traces of Models

Figure 16 shows the 1D power spectra of the models in four panels representing the different ζ values. In each panel, the order from top to bottom of the plotted power spectra is an order of increasing thickness on the line of sight: the single pixel result is at the top, and the $H = 0.125, 0.5, 2$, and 8 cases follow. The dashed line is the observed LMC power spectrum from the integrated map, which was also shown as a dashed line in the middle plot of Figure 3. It is drawn twice in each panel to allow easy comparison with the model results. The dotted line is the $(\zeta, H) = (5, 2)$ exponential disk case shown at the bottom of figure 15. Not all of the model PS fit the observations. Those which do are the models with $(\zeta, H) = (3, 2)$ and $(5, 2)$. The difference between the exponential disk case and the sharp-edge case for the same (ζ, H) is apparent only at very low frequency. Thus the sharp edges in most of the fractal models do not affect our interpretation of the curvature in the power spectra.

Figure 17 shows a horizontal trace of intensity from the middle of each model map, made in the same way as in Figure 11. The observations are reproduced in the top right of this figure, and a range of models is on the left. Each panel on the left shows a different ζ value, and each line shows a different H , taken to be the $H = 0.125, 2$ and 8 models. The $H = 0.125$ results have the largest amplitudes and are represented by solid lines, while the $H = 8$ lines have the lowest amplitudes and are represented by dotted lines. The amplitude of the variation in the intensity trace decreases with increasing depth over the line of sight because the additional random HI washes out the total emission on a deep line of sight. The amplitude variation also decreases with decreasing ζ because the density fluctuations are smaller when the Mach number is smaller.

The right hand side of Figure 17 shows again the H values from the left that reproduce best the observed amplitude of the HI intensity variation. The amplitude variation is about a factor of ten. All of the curves on the right are to the same scale as the LMC intensity strip in both pixel resolution and amplitude. All of the curves also use exactly the same strip in the model fractal, so the variation among them is entirely from the variations in ζ and H , and not from a variation in the noise distribution in wavenumber space.

The top four left-hand panels in Figure 17 are for this standard fractal ISM model. The bottom panels are for a model with a simulated two-phase HI structure, as discussed below. The best fit models in the standard cases have $(\zeta, H) = (3, 0.125), (5, 2)$, and $(9, 8)$, as shown on the right. An increase in ζ gives more density contrast and an increase in H gives less column density contrast, so ζ and H increase together to give the same overall column density contrast.

The only standard fractal model that fits both the 1D power spectrum of the observations and the amplitude of the intensity variations in the LMC data is the model with $(\zeta, H) = (5, 2)$. This is the model shown previously on the top of Figure 15. Generally this model is a good fit to the LMC, in terms of power spectrum and intensity fluctuations. The character of the intensity strip is a good match too, with similar excursions on both large and small scales. This latter point is shown in Figure 12, where the distribution functions for pixel values in the LMC data (left) and the fractal model (right) with $(\zeta, H) = (5, 2)$ are shown in various coordinate systems. The approximately Gaussian character of the pixel distribution of the

observed HI intensity is also present in the model intensity distribution.

The standard fractal model differs from the real LMC in several ways, however. The model lacks the obvious filaments, holes, and shells that are seen by eye in the LMC, and it lacks the sharp transitions from bright to dim that are seen in the LMC intensity strip of Figure 11. These sharp transitions may be phase transitions in the HI, or they could be shock fronts. They contribute only a small fraction of the total LMC HI luminosity, and so do not influence the power spectrum much. They are probably related to the mechanisms of cloud formation however, and are therefore important physically.

4.3. Model with Two Thermal Phases

There is another difference between the model results and the observations and that is the Mach number corresponding to the best-fit case, with $\zeta = 5$. According to equation 3, the Mach number is extraordinarily large, $\sim 10^9$. This is an absurd result and it indicates that the model, even with a turbulence-quality in terms of density distribution, does not contain all of the physics of the real LMC. The real HI distribution has much larger column density variations than can possibly come from homogeneous turbulence alone. Much of the observed variation has to come from other causes, such as phase transitions making low intensity levels all along certain lines of sight, and sharply delineated shock fronts that do the same. A more reasonable Mach number would have $\zeta \sim 1$, but then the amplitude variation of the intensity strip is too small by a factor of ~ 3 , according to the curves in the top left of Figure 17. The remaining factor of ~ 3 in the observed intensity variation probably comes from phase transitions in the HI gas and other density fluctuations independent of pure turbulence compression.

We simulated the additional density structure from HI phase transitions in a fractal ISM model with an effective low Mach number by converting the pixel density values obtained from the previous fractal model, $\rho_0 = \exp(\zeta X)$, into a two-phase density structure using a convenient transformation

$$\rho_{\text{two phase}} = \frac{1}{\rho_0^{-6} + \rho_0}. \quad (6)$$

This transformation is shown in Figure 18. High pixel values, representing high-density clouds, are not changed much, while low pixel values, representing the intercloud medium, are reduced to much lower values. The intensity traces from this two-phase model are shown at the bottom of Figure 17; the $H = 0.125, 2$ and 8 cases are on the left, as before, and the $H = 1$ case is on the right as a best fit to the observed amplitude variation. A low value of $\zeta = 1.4$ was assumed.

The 1D power spectra of the two-phase models are in Figure 19. The values of H used previously in Figure 16 are used again here, as solid lines, but now the case with $H = 1$ pixel is also shown as a dotted line because that is the best fit in Figure 17. A map of the column density structure for the two-phase model with $(\zeta, H) = (1.4, 1)$ looks essentially the same as the map in Figure 15 and is not shown.

For the value of $\zeta = 1.4$ in the two-phase model, the Mach number from equation (3) equals 9.5, which is a reasonable value for a galaxy disk. Higher values of the power in the denominator of equation (6), as well as smaller values of H , give the same intensity variations with lower ζ .

4.4. Two-Dimensional Power Spectra and Delta Variances of the Two-Phase Models

Two-dimensional power spectra of the two-phase models are shown in Figure 20, compared to the 2D PS of the integrated map, which is a dashed line plotted twice for clarity. All the PS have been normalized to have unit value at the lowest wavenumber, and they have been shifted vertically in the plot for clarity. The order of the model PS is, from top to bottom: single channel integral, $H = 0.125, 0.5, 1, 2$, and 5 , with $H = 1$ shown as a short-dashed line, as in Figure 19. Again, the models with low H have too shallow a power spectrum at low frequency, and the models with large H have slightly too steep a power spectrum at low frequency. The $H = 1$ pixel case (corresponding to ~ 10 pc) is about right. The power law for the real LMC data depends on several major asymmetries, such as the enhanced brightness south of the 30 Dor region. These are not present in the fractal model, so the lowest few frequency points on the dashed (LMC) line of Figure 20 are not expected to fit the model well. The rest of the model is reasonably good though.

The Delta variances of the two-phase models are shown as solid lines in Figure 21. The dashed line is the Delta variance for the LMC from Figure 9. The line-of-sight depth increases as the model curves go from top to bottom. The top curve has a single channel in depth, and another at essentially the same place has a Gaussian width on the line-of-sight equal to 0.125 pixel. The remaining have Gaussian widths of $0.5, 1, 2$, and 8 pixel, as in the previous figures. The slope of the Delta variance at small scales is 2 different from the slope of the power spectrum, as expected, and it is in good agreement with the Delta variance for the observations. The model slopes fall for larger scales, presumably because of the growing importance of a few large features inside an ever-decreasing boundary (e.g. Stützki et al. 1998).

5. Conclusions

The structure of HI in the LMC shows the same scale-free character in two-dimensional power spectra as it does in the SMC (Stanimirovic et al. 1999), but it steepens at short wavelengths in the one and two-dimensional power spectra, and in the azimuthal power spectra, perhaps as a result of a transition to a relatively thick disk on that scale. Such steepening has been predicted for such a transition from thin to thick lines of sight (Lazarian & Pogosyan 2000), but its importance as a potential indicator of extragalactic disk thickness was not previously recognized.

The power spectrum of the whole galaxy resembles the power spectra of individual channel maps in the regions where the channel maps trace the velocity centroids of the emission. This implies that individual channels contain essentially the same structure as the whole spectral line at the spatial position where the centroid of the line has the same velocity as the channel map. Narrow velocity slices do not come from a thinner region than the whole spectral line, for example, and the small scale structure in the ISM is not limited to any particular part of the line profile. This conclusion is based only on our study of very large regions and does not necessarily apply to all lines of sight. Expanding shells should deviate from this trend, of course, because the small near- and far-side caps should appear in different parts of the spectral line than the large projected circumference.

The character of the HI structure was also investigated using positive and negative images to compare the high and low emission regions, and using unsharp masks with four different resolutions. On all scales between ~ 30 and ~ 400 pc, the emission tends to be filamentary, and the regions between the emission tend to be round. This is what might be expected from a conglomerate of expansion sites, although the nature of the high pressure that drives each expansion is not indicated. For example, the high pressure could be stellar in origin, or it could come from turbulent fluctuations.

Fractal models of a face-on galaxy with a log-normal probability distribution function for local density and a Gaussian distribution of density on the line of sight reproduce the observations fairly well. The models get the power spectrum of the LMC, the peak-to-peak amplitude of the emission variations, and the probability distribution function for pixel values. The models suggest that most of the spatial structure in the HI is in a relatively thin midplane layer, perhaps ~ 50 pc thick. This implies that any thicker HI layer that surrounds the cloudy disk has relatively little structure; i.e., most of the LMC clouds are in a cool component of the HI that has a relatively low velocity dispersion and a low scale height.

The models include a log-normal distribution for local density in order to simulate compressible isothermal turbulence. The model can be tuned to the observations by adjusting the Mach number of the turbulence, which enters into the Gaussian dispersion of the log-normal, and the thickness of the disk. The best fits require unrealistically large Mach numbers, so other models were made having additional HI structure from a simulated phase transition between warm and cool HI components. These models could be tuned to fit the LMC data with a more realistic Mach number.

Positional fluctuations in the power spectra are slightly larger at larger scales, suggesting that significant energy is put into the interstellar medium on kiloparsec scales, probably in connection with the well-known supershells. However, the positional fluctuations are still fairly large on smaller scales, amounting to 0.2-0.3 dex, so there are either additional energy sources on small scales, or quick and local cascades of supershell energy to smaller scales. A power-law distribution of shell sizes (Oey & Clarke 1997) may provide the range of scales necessary.

The power spectra of HI emission at large scales in the LMC are slightly shallower than the power spectra of foreground Milky Way emission. Presumably the foreground emission is thick on the line of sight, relative to the largest transverse wavelength, as is the short wavelength emission from the LMC. The similarity of the power spectra for thick emission is remarkable considering the factor of ~ 200 difference in physical scales.

We would like to acknowledge the encouragement and advice of Dr. Agris Kalnjas at Mount Stromlo Observatory in Australia. Helpful comments on the Delta variance by Drs. Ossenkopf and Mac Low, and on the power spectra of turbulent gases by Dr. Lazarian, are also appreciated. This work was supported by NSF Grant AST-9870112 to B.G.E.

REFERENCES

- Abergel, A., Boulanger, F., Delouis, J.M., Dudziak, G., & Steindling, S. 1996, *A&A*, 309, 245.
- Bazell, D., & Désert, F. X. 1988, *ApJ*, 333, 353
- Beech, M. 1987, *ApSpSci.*, 133, 193
- Berkhuijsen, E.M. 1999, in *Plasma Turbulence and Energetic Particles in Astrophysics*, eds. M. Ostrowski, & R. Schlickeiser, Krakow: Uniwersytet Jagiellonski, p. 61
- Carignan, C. & Purton, C. 1998, *ApJ*, 506, 125
- Crovisier, J., & Dickey, J.M. 1983, *A&A*, 122, 282
- Dickman, R. L., Horvath, M. A., & Margulis, M. 1990, *ApJ*, 365, 586
- Elmegreen, B.G., 1997, *ApJ*, 477, 196
- Elmegreen, B.G., 1999, *ApJ*, 527, 266

- Elmegreen, B.G., & Falgarone, E. 1996, *ApJ*, 471, 816
- Falgarone, E., Phillips, T. G., & Walker, C. K. 1991, *ApJ*, 378, 186
- Green, D.A. 1993, *MNRAS*, 262, 327
- Hodge, P.W., & Hitchcock, J.L. 1966, *PASP*, 78, 79
- Kim, S., Staveley-Smith, L. & Dopita, M. A. 1998a, in *The Magellanic Clouds and Other Dwarf Galaxies*, ed. T. Richtler and J.M. Braun, Aachen: Shaker Verlag, p. 169
- Kim, S., Staveley-Smith, L., Dopita, M.A., Freeman, K.C., Sault, R.J., Kesteven, M.J., McConnell, D. 1998b, *ApJ*, 503, 674
- Kim, S., Dopita, M.A., Staveley-Smith, L., Bessell, M.S. 1999, *AJ*, 118, 2797
- Kim, S., & Staveley-Smith, L., & Sault, R.J. 2000, *astro-ph/0009299*
- Kulkarni, S.R., & Heiles, C. 1987, in *Interstellar Processes*, ed. D. Hollenbach & H. Thronson, Dordrecht: Reidel, 87
- Lazarian, A., & Pogosyan, D. 2000, *ApJ*, 537, 720
- MacLow, M.M., & Ossenkopf, V. 2000, *A&A*, 353, 339
- Mandelbrot, B.B. 1983, *The Fractal Geometry of Nature*, (San Francisco: Freeman)
- Marx-Zimmer, M., Herbstmeier, U., Dickey, J. M., Zimmer, F., Staveley-Smith, L., & Mebold, U. 2000, *A&A*, 354, 787
- Meaburn, J. 1980, *MNRAS*, 192, 365
- Nordlund, A., & Padoan, P. 1999, in *Interstellar Turbulence*, eds. J. Franco & A. Carramiñana, Cambridge: Cambridge University Press, p. 218
- Oey, M.S., & Clarke, C.J. 1997, *MNRAS*, 289, 570
- Pichardo, B., Vázquez-Semadeni, E., Gazol, A., Passot, T., Ballesteros-Paredes, J. 2000, *ApJ*, 532, 353
- Rosolowsky, E.W., Goodman, A.A., Wilner, D.J., & Williams, J.P. 1999, *ApJ*, 524, 887
- Scalo, J. 1990, in *Physical Processes in Fragmentation and Star Formation*, eds. R. Capuzzo-Dolcetta, C. Chiosi, & A. Di Fazio, Dordrecht: Kluwer, p. 151
- Scalo, J., Vazquez-Semadeni, E., Chappell, D., Passot, T. 1998, *ApJ*, 504, 835
- Scalo, J., & Chappell, D. 1999a, *MNRAS*, 310, 1
- Scalo, J., & Chappell, D. 1999b, *ApJ*, 510, 258
- Sreenivasan, K.R. 1991, *Ann.Rev.Fluid Mech.*, 23, 539
- Stanimirovic, S., Staveley-Smith, L., Dickey, J.M., Sault, R.J., & Snowden, S.L. 1999, *MNRAS*, 302, 417
- Staveley-Smith, L., Davies, R. D., & Kinman, T. D. 1992, *MNRAS*, 258, 334
- Staveley-Smith, L., Wilson, W. E., Bird, T. S., Disney, M. J., Ekers, R. D., Freeman, K. C., Haynes, R. F., Sinclair, M. W., Vaile, R. A., Webster, R. L., & Wright, A. E. 1996, *PASA*, 13, 243
- Stutzki, J., Bensch, F., Heithausen, A., Ossenkopf, V., & Zielinsky, M. 1998, *A&A*, 336, 697
- van den Bergh, S. 1988, *PASP*, 100, 344
- Vazquez-Semadeni, E. 1994, *ApJ*, 423, 681
- Vogelaar, M. G. R., & Wakker, B. P. 1994, *A&A*, 291, 557

- Voss, R. 1988, in *The Science of Fractal Images*, eds. H.O. Peitgen, & D. Saupe, New York: Springer
- Wada, K., Spaans, M., & Kim, S. 2000, *ApJ*, 540, 797
- Wang, Q., & Helfand, D.J. 1991, *ApJ*, 379, 327
- Westpfahl, D.J., Coleman, P.H., Alexander, J., Tongue, T. 1999, *AJ*, 117, 868
- Young, L. M., & Lo, K. Y. 1996, *ApJ*, 462, 203
- Young, L. M., & Lo, K. Y. 1997, *ApJ*, 490, 710
- Zielinsky, M., & Stützki, J. 1999, *A&A*, 347, 630

Figure Captions

Fig. 1.— Four images of HI emission from the LMC, each with 3×3 subfields for separate power spectrum analyses. Top left: peak HI temperature; top right: HI integrated over velocity; Lower left: channel map at $254 \pm 0.8 \text{ km s}^{-1}$; lower right: channel map at $302 \pm 0.8 \text{ km s}^{-1}$. The giant HII region 30 Dor is in the middle subfield on the left; the supershell LMC4 is on the white line dividing the top left and middle subfields. (see jpg file for astroph)

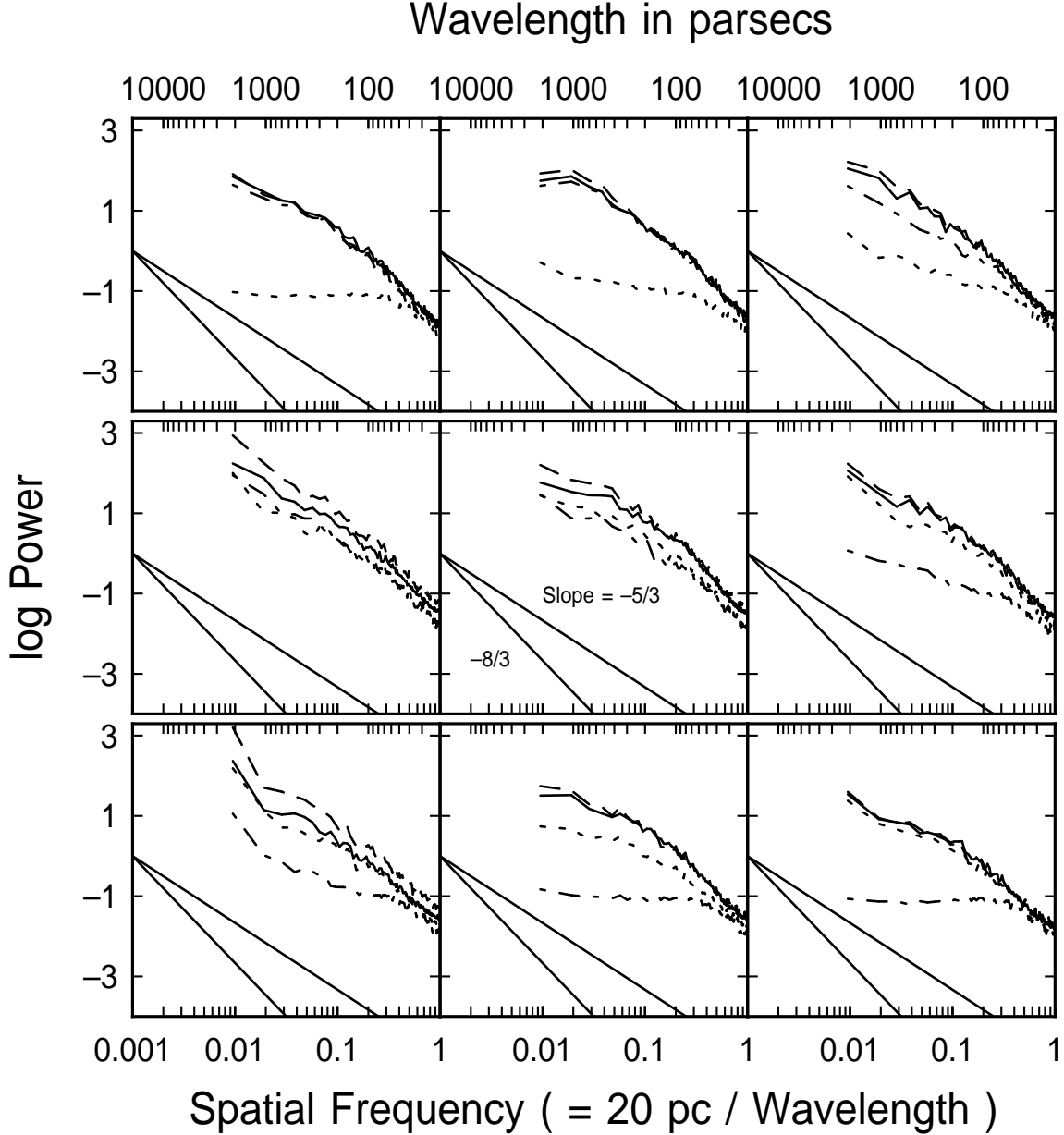


Fig. 2.— Average, one-dimensional power spectra of the HI emission from each of the 3×3 panels in figure 1, shown here in a similar 3×3 array with the same orientation (North up). Lines types denote the various HI maps shown in Figure 1: solid = peak temperature map, dashed = velocity integrated map, dotted = 254 km s⁻¹ channel map, and dot-dashed = 302 km s⁻¹ channel map. Kolmogorov turbulence is expected to give a 1D Power spectrum with a slope of $-5/3$ if the region observed is thinner on the line-of-sight than the transverse wavelength. This is the slope seen here at small wavenumbers. The same turbulence is expected to give a 1D Power spectrum with a steeper slope of $-8/3$ if the region is thicker on the line-of-sight than the wavelength, and this is what the figure suggests for wavenumbers exceeding 0.2. The dividing point corresponds to a wavelength of ~ 100 pc, which is suggested to be a measure of the line-of-sight thickness of the HI layer in the LMC.

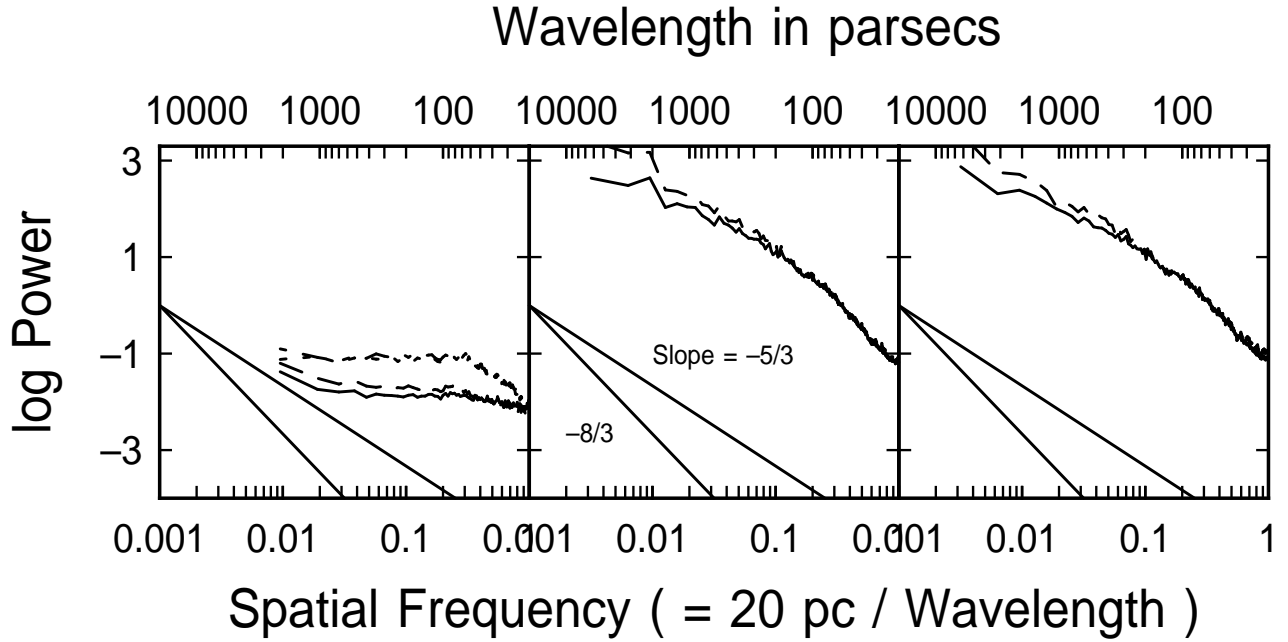


Fig. 3.— Left: Average, one-dimensional power spectra of the HI emission from the sky region shown in figure 4; middle: average 1D power spectrum for the whole galaxy, using 1D FFTs in the horizontal (E-W) direction, and, right: power spectrum of the whole galaxy using 1D FFTs in the vertical (N-S) direction. Line types are as in Fig. 2.

Fig. 4.— HI emission from the Northeast corner of the velocity-integrated map, showing a box in which the power spectrum of the sky was calculated. (see jpg file for astroph)

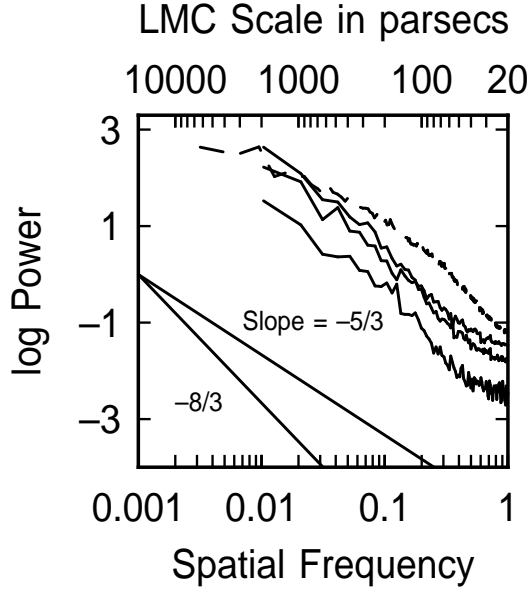


Fig. 5.— Power spectra of foreground HI emission from the Milky Way in three different velocity channels. The HI power spectrum is generally steeper for foreground emission than it is for the low wavenumber part of the LMC emission, but it is similar to the high-wavenumber part of the LMC, suggesting that the foreground emission in each velocity channel is physically thick on the line of sight, like the LMC at short wavelengths.

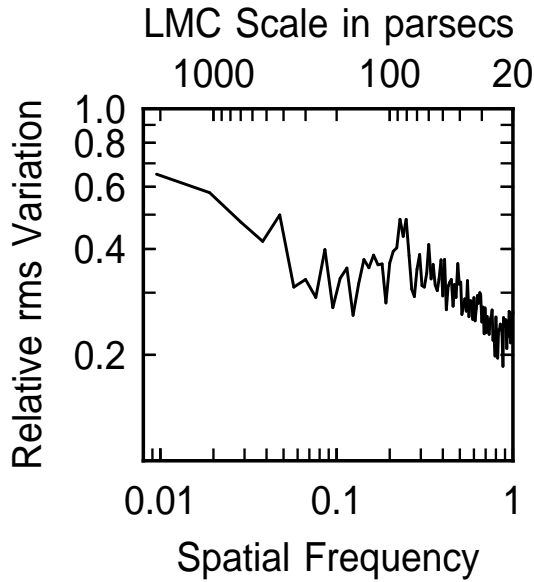


Fig. 6.— Relative rms variations in the power spectra among all nine subfields shown in figures 1 and 2. The relative rms variation is largest on largest scales, to the left in the diagram, presumably because turbulent energy is put into the interstellar medium on these scales.

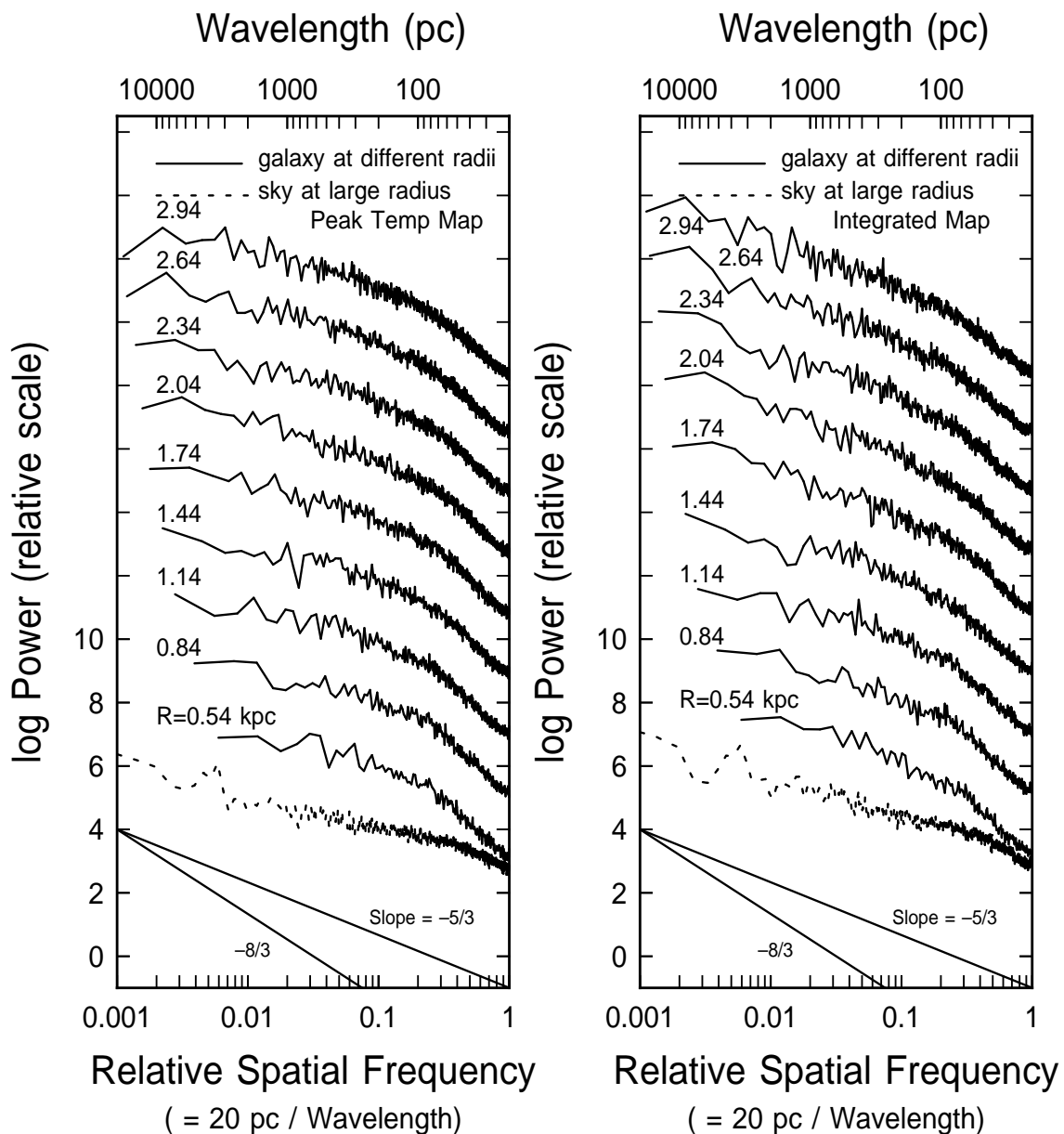


Fig. 7.— Power spectra of the HI emission from the LMC taken in deprojected azimuthal scans around the center of the galaxy to remove the possible effects of the radial disk gradient. The panel on the left is for the peak temperature map, and the panel on the right is for the integrated map. Radii in kpc for each azimuthal scan are given next to the corresponding curve. The dashed line is from a sky region at 9.3 kpc, shown on the same scale as the azimuthal power spectrum for 0.54 kpc. The slope of the one-dimensional azimuthal power spectrum is $\sim -5/3$ at small wavenumbers and $\sim -8/3$ at large wavenumbers, the same as it is for the East-West and North-South scans, indicating again some possible sensitivity to the line-of-sight thickness of the HI layer in the LMC. The wavelength of this steepening point increases slightly with galactocentric radius, as if the disk thickness increases with radius too.

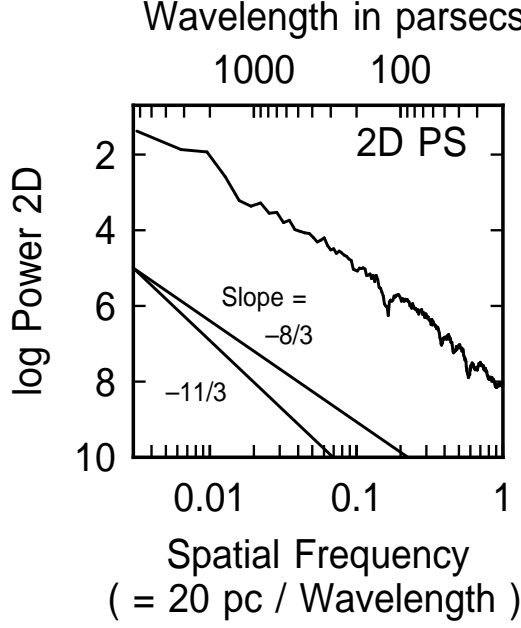


Fig. 8.— Two-dimensional power spectrum of the LMC integrated emission.

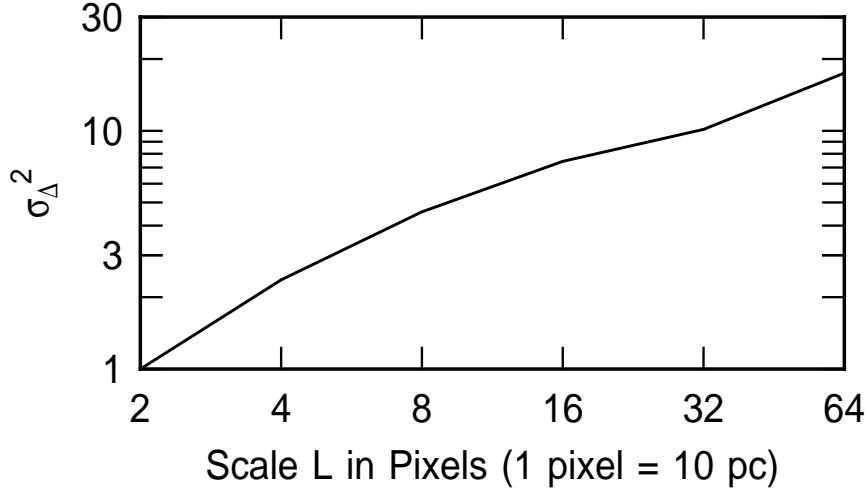


Fig. 9.— Two-dimensional Delta variance of the LMC integrated emission.

Fig. 10.— Colorized emission maps of a central region of the LMC, showing white HI emission on a blue background at the bottom of the figure, and the reverse colors at the top. The difference in morphology of the white regions in these two images illustrates the difference between the cloud geometry and the intercloud geometry. The clouds are often filamentary, while the intercloud medium is often globular. This difference suggests the HI structure is made by expansion around intercloud centers, either from turbulence or from point sources of energy. (see jpg image for astroph)

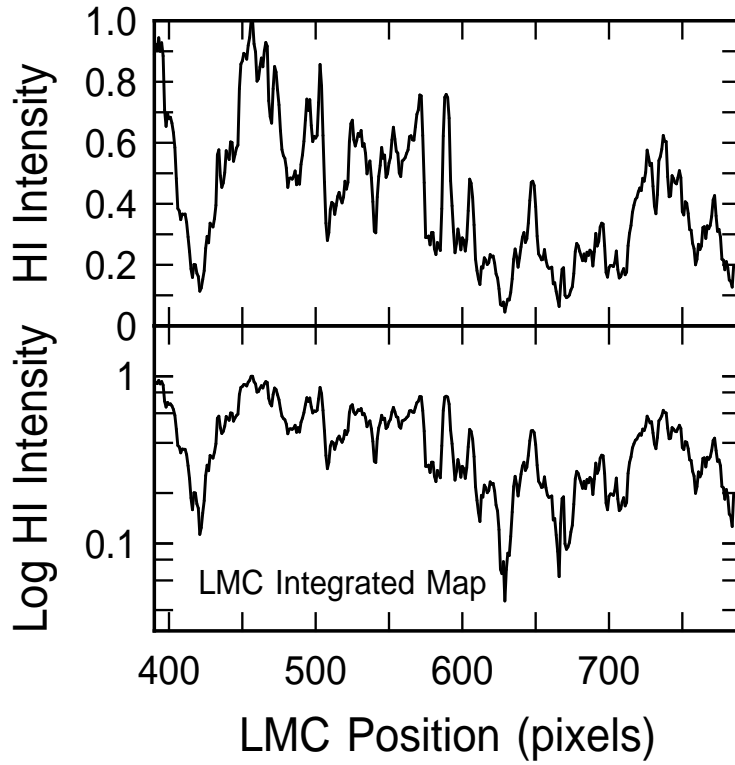


Fig. 11.— An HI intensity strip from the central region of the LMC field in figure 10, shown in linear and logarithmic coordinates. The fluctuations around the mean are more symmetric and random-looking on the logarithmic plot, illustrating the peaked-nature of the emission regions, and the broad nature of the intercloud regions.

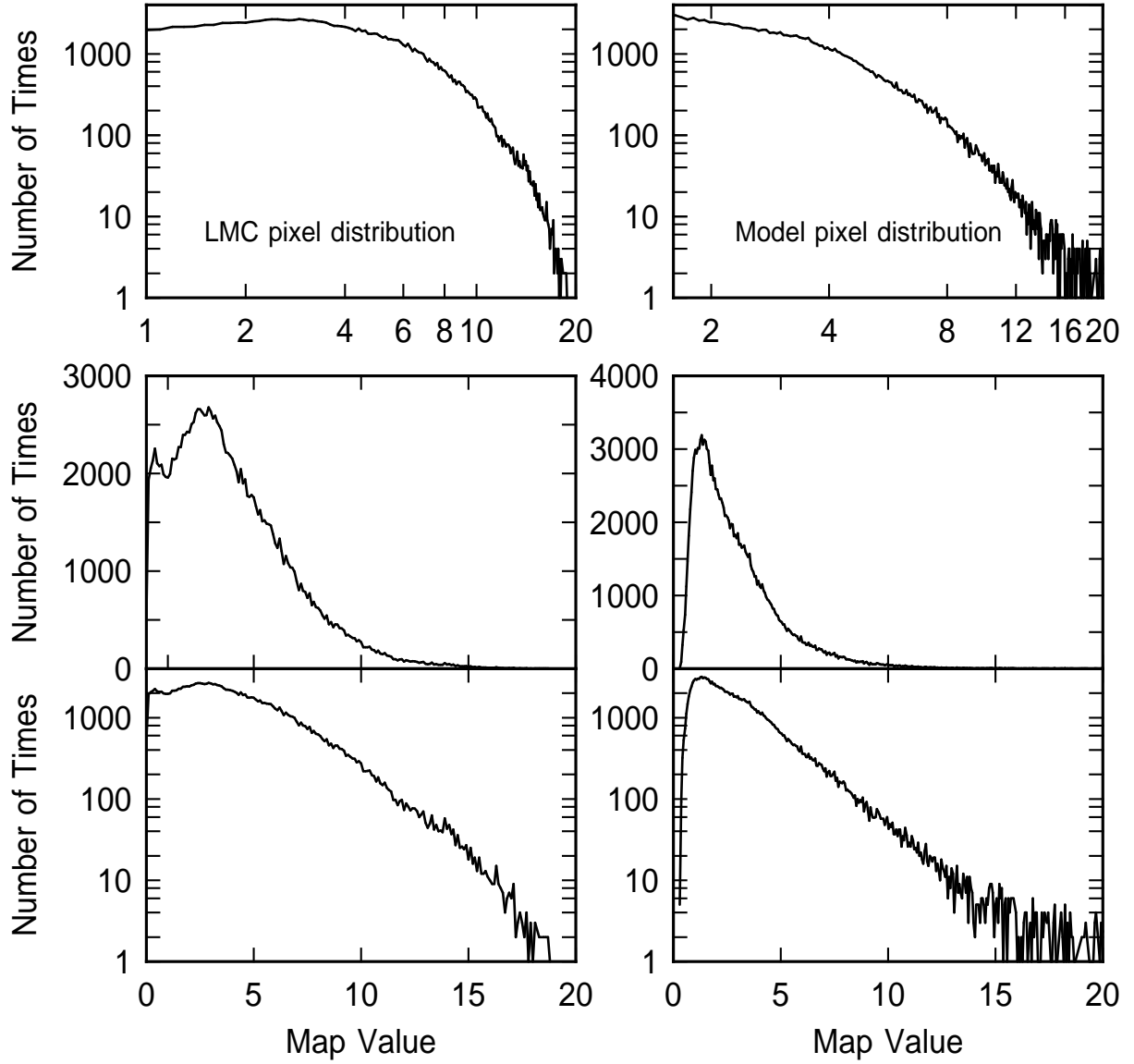


Fig. 12.— (Left:) Histograms of the pixel values in a 400×400 pixel field centered on the region shown in figure 10. The diagrams are plotted in log-log, linear-linear, and log-linear coordinates. (Right:) Histograms of the pixel distribution in the fractal model shown on the top of figure 15.

Fig. 13.— Unsharp masks of the integrated HI emission from the whole LMC, emphasizing features on scales of 30 pc, 110 pc, 210 pc, and 410 pc. (see jpg image for astroph)

Fig. 14.— Expanded versions of the high resolution unsharp mask in the upper left, which is reproduced from figure 13. The expansions give the other maps here the same pixel resolution as the corresponding maps in figure 13. The character of the emission, with circular holes surrounded by filamentary emission, is approximately the same on all of the scales shown, which range from 30 pc to 410 pc. (see jpg image for astroph)

Fig. 15.— top: Column density map of a standard model fractal ISM measuring 630x630 pixels. The model has a Gaussian density distribution on the line of sight with a dispersion of $H = 2$ pixels to represent the thin layer of a face-on galaxy. A turbulence parameter representing Mach number has the value $\zeta = 5$. The density in each pixel of the volume fractal is given by $\exp(\zeta X)$ for a fractal field X generated from the inverse Fourier transform of noise with a power-law cutoff. The two-phase model looks about the same as this. bottom: The same model with an exponential taper having four scale lengths to the edge. (see jpg image for astroph)

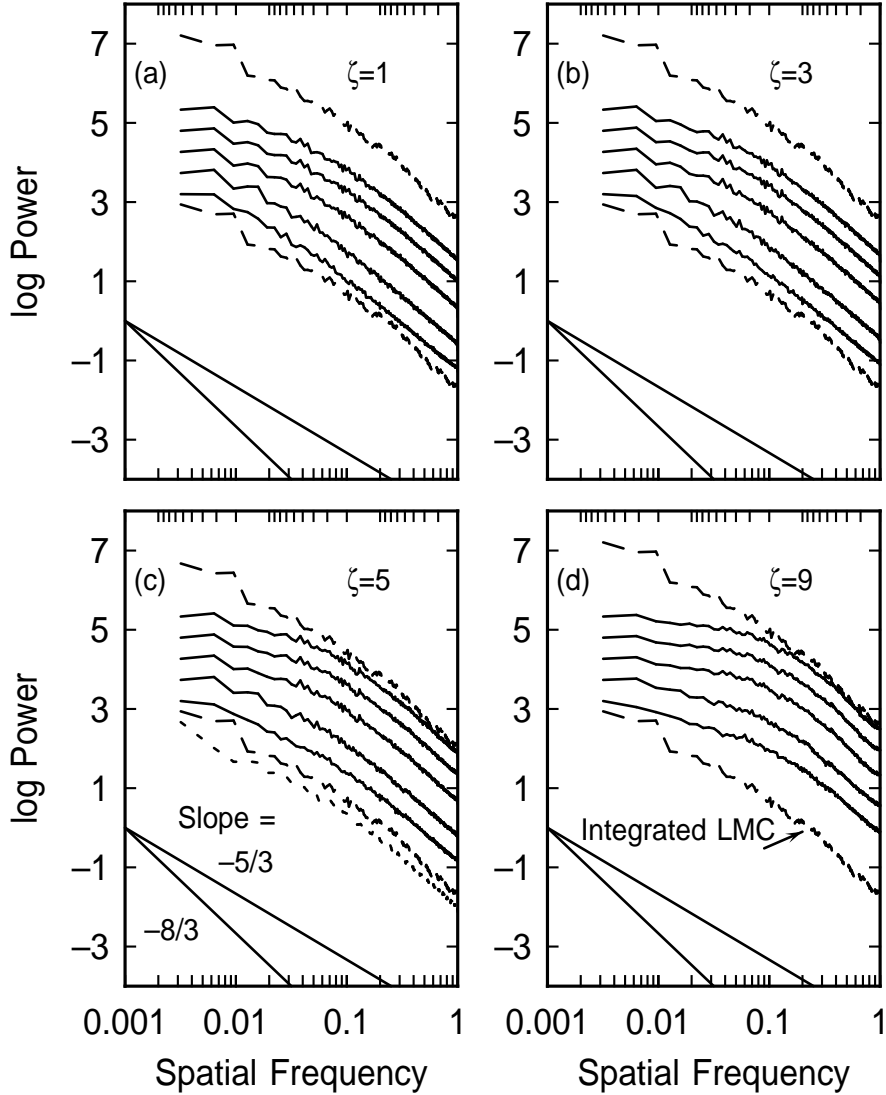


Fig. 16.— Power spectra of the model fractal ISMs compared with the observed power spectrum from the velocity-integrated map. The dotted line in the lower right panel is for the model with an exponential disk. It resembles the preferred model with the same parameters, $(\zeta, H) = (5, 2)$, which is the second line up from the dashed line, at all but the lowest frequencies.

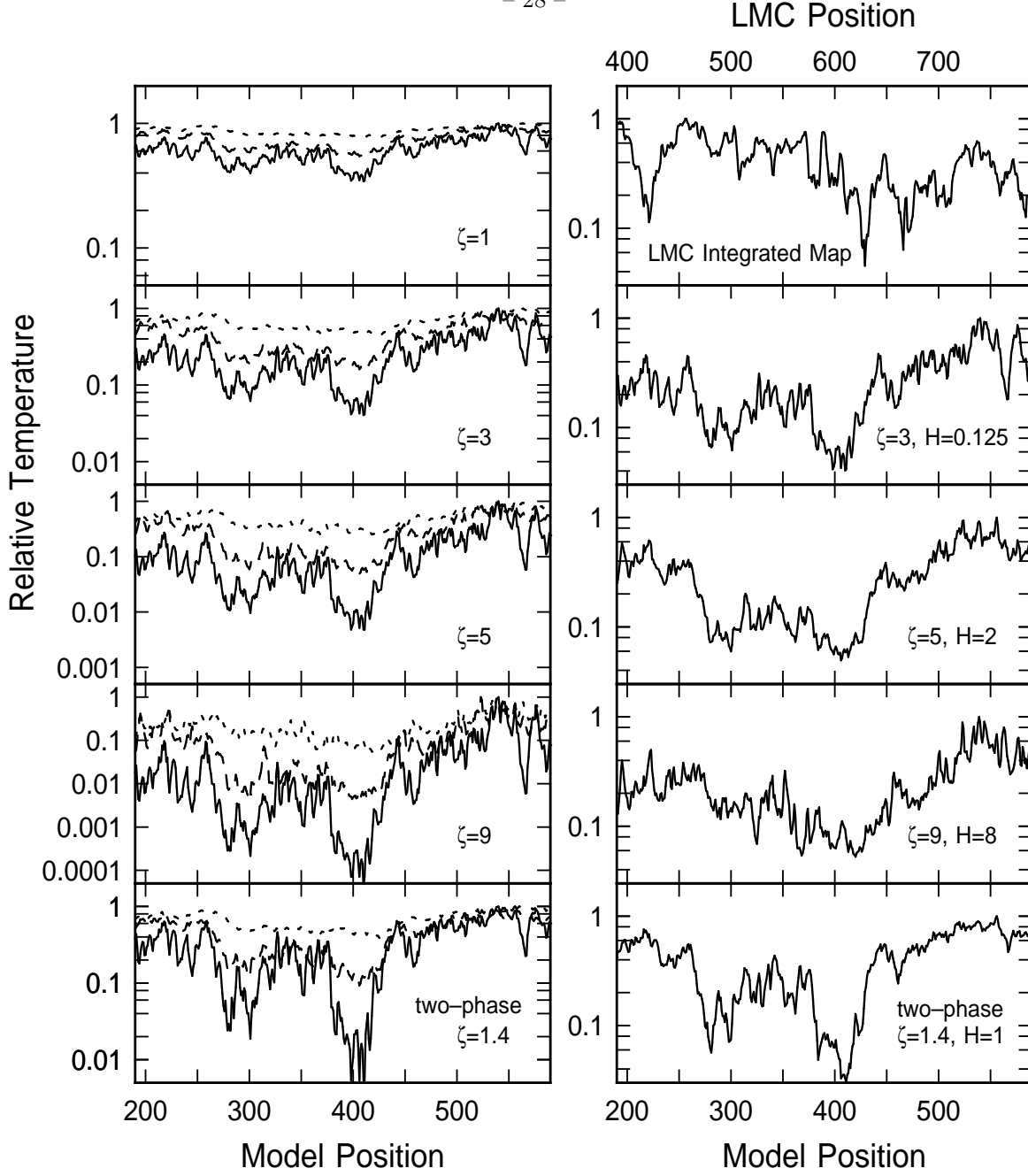


Fig. 17.— Intensity traces from various fractal models compared to the observed HI intensity trace (top right) from the field in figure 10, also shown in figure 11. The dotted, dashed and solid lines on the left are for models with different scale heights in the Gaussian representation of the face-on galaxy: $H = 0.125$, 2 , and 8 , respectively. The different panels are for different Mach number parameters, ζ , with larger ζ representing larger Mach numbers. Acceptable models have intensity fluctuations of a factor of ~ 10 , and are shown on the right for each Mach number parameter, ζ . The bottom panels are for the model with a simulated two-phase medium.

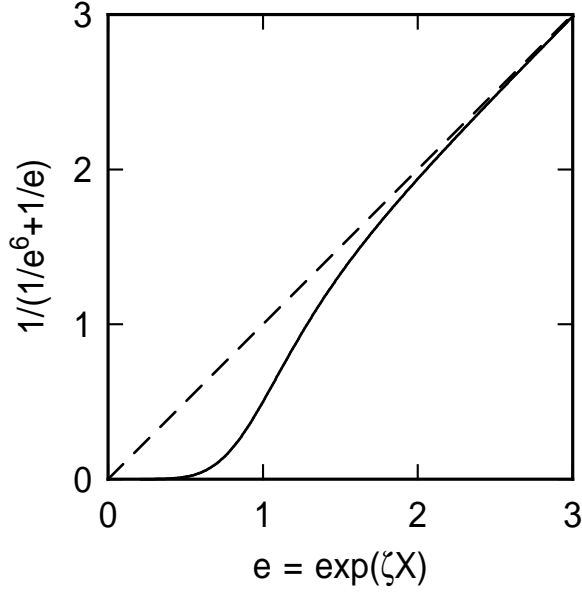


Fig. 18.— Transformation of density in the original fractal model, $\rho_0 = \exp(\zeta X)$, into density in a simulated two-phase model, $\rho_{\text{two phase}}$. Low values of the original density are converted into very low values in the two-phase model, while high values are not changed much.

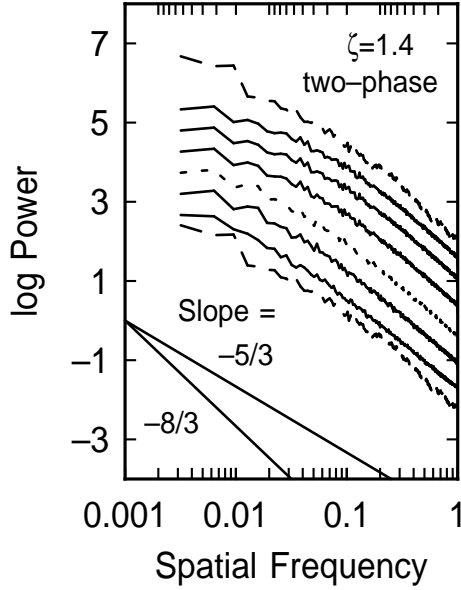


Fig. 19.— Power spectra of the models with simulated two phases, as in figure 16.

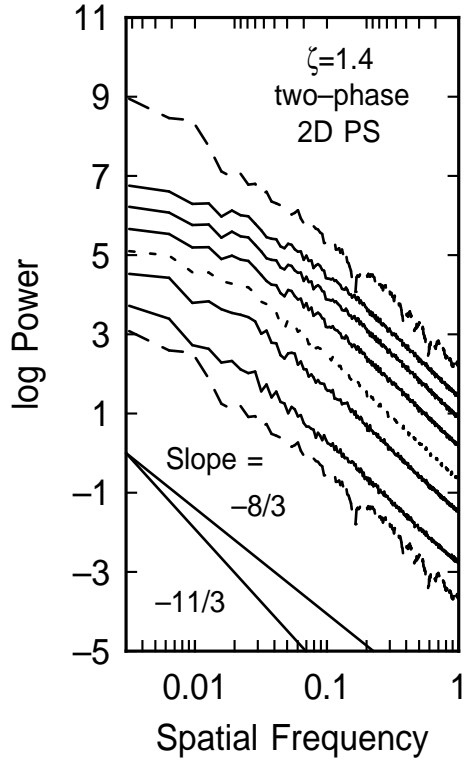


Fig. 20.— Two-dimensional power spectra of the models with simulated two phases.

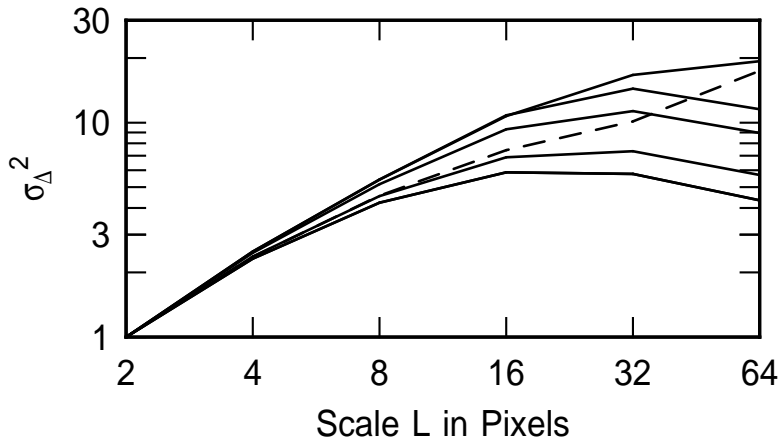


Fig. 21.— Two-dimensional Delta variances of the models with simulated two phases.

This figure "elmegreen_fig1.jpg" is available in "jpg" format from:

<http://arxiv.org/ps/astro-ph/0010578v1>

This figure "elmegreen_fig4.jpg" is available in "jpg" format from:

<http://arxiv.org/ps/astro-ph/0010578v1>

This figure "elmegreen_fig10.jpg" is available in "jpg" format from:

<http://arxiv.org/ps/astro-ph/0010578v1>

This figure "elmegreen_fig13.jpg" is available in "jpg" format from:

<http://arxiv.org/ps/astro-ph/0010578v1>

This figure "elmegreen_fig14.jpg" is available in "jpg" format from:

<http://arxiv.org/ps/astro-ph/0010578v1>

This figure "elmegreen_fig15.jpg" is available in "jpg" format from:

<http://arxiv.org/ps/astro-ph/0010578v1>